

Research Article

Application of Motion Capture Based on Digital Filtering Algorithm in Sports Dance Teaching

Fan Rao 

College of Physical Education, Hunan Normal University, Changsha 410012, China

Correspondence should be addressed to Fan Rao; 16390@hunnu.edu.cn

Received 10 March 2022; Revised 28 April 2022; Accepted 9 May 2022; Published 29 May 2022

Academic Editor: Qiangyi Li

Copyright © 2022 Fan Rao. This is an open access article distributed under the Creative Commons Attribution License, which permits unrestricted use, distribution, and reproduction in any medium, provided the original work is properly cited.

In order to improve the teaching effect of sports dance, this paper analyzes the traditional dance teaching motion capture, uses sensor motion perception algorithms to capture sports dance motion perception, and designs an intelligent sensor system that can be used for sports dance motion capture. Moreover, this paper combines the digital filter algorithm to design the hardware system structure of the sports dance motion capture system and builds a motion capture system for sports dance teaching based on the digital filter algorithm according to actual needs. In addition, this paper combines the simulation test to evaluate the performance of the system designed in this paper. The research results show that the motion capture system for sports dance teaching based on the digital filtering algorithm proposed in this paper can play an important role in sports dance teaching and effectively improve the efficiency of sports dance teaching.

1. Introduction

The motion capture system was first applied to animated films and gradually expanded to be applied to the training system of athletes, sports analysis, etc. The motion capture system is mainly composed of sensors, signal acquisition equipment, data transmission, and data processing. These are mechanical, electromagnetic, and optical. The sports dance data collected by the motion capture system is input into the 3D animation software and can be perfectly displayed through the virtual display engine. Motion capture technology is a technology that turns human motion information into a computer that can be recognized [1]. The captured data can convert the human body's movements in real three-dimensional space into virtual three-dimensional space data on the computer. The motion capture system first captures the motion of the human body and then maps the captured motion to a computer-generated virtual model [2]. The object of motion capture is the motion of the model. It pastes special mark points "Marker" on the joint points of the model and then uses the capture lens of the motion capture device to sample the position of these mark points in space, thereby generating a set of motion data that can be

recognized by the computer. Once we have the motion data, we can enter the 3D animation software and build the 3D human body model in the 3D animation software. Each three-dimensional model is a polygonal mesh model, which simulates the dancer's standard body as much as possible, and the facial features also adopt the main facial features of various ethnic groups [3].

After the establishment of the human body model, clothing and apparel models must be established; various sports dances and national costumes are different, so it is necessary to establish multiple sets of clothing and apparel models distinguished by men and women. After the above model is established, it is necessary to create a three-dimensional skeleton that accurately corresponds to the model to prepare for the next step of skinning. Skinning is to combine the bones with the model so that the model and the bones are bound together correctly. At the same time, the binding of various clothing and apparel should be done, and then the data collected by the motion capture system should be imported and combined with the three-dimensional animation. The combination of bones drives the 3D model to generate animation. These animations can be easily imported into the virtual presentation platform and can also be

rendered into video files for presentation, saving, etc., in preparation for subsequent applications.

The emergence of various information technologies has brought innovation power to the development of art forms. Virtual technology is the simulation of real scenes, and its design, display, and viewing technology are becoming more and more mature. For art education, virtual reality provides new opportunities for the construction and display of professional courses. College teachers should take the initiative to accept the challenges brought by new technologies, design more suitable and interesting courses for students, and bring them to art education. Innovation. Sports dance education usually uses on-site teaching, and students generally comprehend the knowledge and skills of sports dance by imitating the movements of the teacher. General online course teaching is only a two-dimensional display of knowledge, and the simple interaction between teachers and students is not suitable for sports dance education.

This article combines the digital filter algorithm to construct the motion capture system of sports dance teaching, changes the current sports dance teaching method, applies intelligent teaching to the motion capture of sports dance, and improves the teaching effect of sports dance.

2. Related Work

Segmentation is based on simple actions, so-called simple actions, such as raising hands, raising legs, etc. Based on the idea of kinematic characteristics, the change of linear velocity, angular velocity, acceleration, energy, and other characteristics are used to determine the position of the split point. Reference [4] used angular velocity as the segmentation feature to determine the motion boundary by using the angular velocity zero crossing (ZVC) method to determine the motion boundary, calculate the sum of the angular velocity of each joint point on the arm, and set the threshold for comparison to determine the split point. Literature [5] uses the method of calculating the linear acceleration zero-crossing point and the curvature to segment the hand motion boundary, and the point where the calculation result is greater than the set threshold is the segmentation point. Literature [6] uses linear velocity as the segmentation feature, taking arm movements as an example, calculates the sum of the linear velocities of joint points, and the points below the set threshold are the segmentation points. Literature [7] is based on kinematics characteristics while considering the changes of linear velocity and curvature. When two features are reduced at the same time, it is defined as a split point. The segmentation algorithm based on kinematic features is very effective for the segmentation of low-level semantic actions. The dimensionality reduction segmentation algorithm based on unsupervised learning adopts the idea of clustering dimensionality reduction. This type of algorithm mainly performs segmentation processing for high-level semantic actions, such as running, window cleaning, and other complex actions. Literature [8] uses three segmentation algorithms based on time series. The first is principal component analysis (PCA), which performs dimensionality reduction processing on motion capture

data, and maps the data from high-dimensional space to low-dimensional space without affecting the original data. Under the premise of information, calculate the projection error and divide the data in the low-dimensional space, which greatly reduces the amount of calculation; the second method is to introduce a probability model on the basis of PCA, calculate the Mahalanobis distance, and determine the division point; the third method is to use the Gaussian mixture model (GMM) segmentation algorithm to obtain the segmentation points by calculating the mathematical expectation maximization. Literature [9] uses the principal component analysis (PCA) segmentation algorithm. Literature [10] proposed the use of a Gaussian mixture model segmentation algorithm based on principal component analysis (PCA), which first uses PCA to reduce the dimensionality of the motion capture data and then calculates the maximum likelihood function of the Gaussian mixture model to achieve clustering segmentation. Literature [11] uses the Gaussian mixture model algorithm based on K-means clustering. Literature [12] proposed an automatic segmentation algorithm for motion capture data based on Kernel Principal Component Analysis (KPCA) dimensionality reduction. Literature [13] uses an algorithm based on KPCA to solve the nonlinear problem by introducing a kernel function and obtain the segmentation point. Literature [14] proposed to use a segmentation algorithm based on probability kernel principal component analysis. Literature [15] proposed nonlinear popular dimensionality reduction technology (ISOMAP), which performs dimensionality reduction processing on high-dimensional human motion data, combined with K-means clustering of similar poses, so as to obtain more accurate segmentation points. Literature [16] uses principal component analysis (PCA) to reduce dimensionality to process data and combines dynamic time warping to obtain the segmentation points of the motion sequence. Segmentation algorithm based on machine learning: Literature [17] proposed a human motion segmentation algorithm based on training Hidden Markov Model (HMM), and literature [18] proposed a segmentation method using singular value decomposition (SVD) to calculate the similarity matrix. Literature [19] proposed a segmentation algorithm based on human action space. Literature [20] uses a simple Bayesian classifier to segment human movements.

3. Digital Filter Sensor Algorithm and Its Structure Design

The magnetic field sensor is based on the Hall effect of semiconductor materials. The Hall element is fabricated on a single crystal silicon substrate to realize the measurement of the magnetic field, and the magnetic sensitive layer adopts an ion implantation process to dope phosphorus elements on the single crystal silicon substrate to form an n-type magnetic sensitive layer.

We apply a certain operating voltage V_{DD} to both ends of the magnetic field sensor control current pole. When the external magnetic field is $B = 0T$, ideally, the carriers in the magnetic sensitive layer will not deflect, the current will be

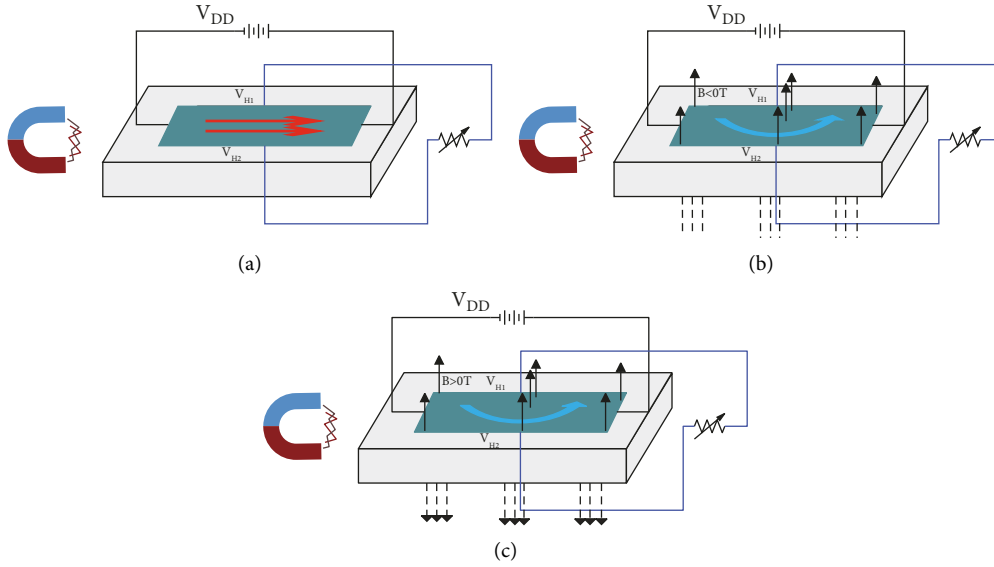


FIGURE 1: Schematic diagram of the working principle of magnetic field sensor: (a) $B = 0T$, (b) $B < T$, (c) $B > OT$.

evenly distributed, and the potentials of the two Hall output terminals will be equal, as shown in Figure 1(a). Ideally, the Hall output voltage V_H is expressed as follows [21]:

$$V_H = V_{H1} - V_{H2} = 0. \quad (1)$$

In the formula, V_{H1} and V_{H2} are the potentials of the two Hall output terminals.

When the applied magnetic field is $B \neq 0T$, the carriers in the magnetic sensitive layer are deflected by the Lorentz force under the action of the applied magnetic field, and there is a potential difference between the Hall output terminals, as shown in Figures 1(b) and 1(c). This article defines the direction of the external magnetic field perpendicular to the chip surface upward as $B < OT$, and the downward perpendicular to the chip surface as $B > OT$. The Hall output voltage changes with the applied magnetic field.

$$V_H = V_{H1} - V_{H2} = \mu \cdot \frac{W}{L} \cdot V_{DD} \cdot B \cdot f_H\left(\frac{L}{W}, \theta\right). \quad (2)$$

In the formula, $f_H(L/W, \theta)$ is the geometric structure factor, L is the length of the magnetic sensitive layer, W is the width of the magnetic sensitive layer, θ is the angle between the direction of the applied magnetic field and the plane of the magnetic sensitive layer, μ is the carrier mobility, B is the magnetic induction intensity of the applied magnetic field, and V_{DD} is the power supply voltage.

From formula (2), the magnetic sensitivity of the magnetic field sensor can be obtained as follows [22]:

$$S = \frac{V_H}{B} = \mu \cdot \frac{W}{L} \cdot V_{DD} \cdot f_H\left(\frac{L}{W}, \theta\right). \quad (3)$$

It can be seen from the above formula that the sensitivity of the magnetic field sensor is related to the carrier mobility and width-to-length ratio of the magnetic sensitive layer and can realize the measurement of the forward and reverse magnetic fields.

When a constant current source is used for the power supply, the Hall output voltage of the magnetic field sensor is as follows:

$$V_H = V_{H1} - V_{H2} = \frac{\rho\mu}{d} \cdot I \cdot B \cdot f_H\left(\frac{L}{W}, \theta\right). \quad (4)$$

In the formula, $f_H(L/W, \theta)$ is the geometric structure factor, ρ is the resistivity, μ is the carrier mobility, d is the thickness of the magnetic sensitive layer, B is the magnetic induction intensity of the applied magnetic field, and I is the power supply current. The sensitivity of the magnetic field sensor is as follows:

$$S = \frac{V_H}{B} = \frac{\rho\mu}{d} \cdot I \cdot f_H\left(\frac{L}{W}, \theta\right). \quad (5)$$

It can be seen from the above formula that the sensitivity of the magnetic field sensor is proportional to the resistivity and carrier mobility of the magnetic sensitive layer and inversely proportional to the thickness of the magnetic sensitive layer.

Based on the piezoresistive effect of semiconductor materials, four piezoresistors are fabricated on the surface of the C-type silicon cup silicon film and connected to a Wheatstone bridge structure. The pressure is measured by measuring the output voltage of the Wheatstone bridge. Figures 2(a) and 2(b), respectively, show the schematic diagram of the working principle of the pressure sensor when there is no applied pressure and when there is applied pressure. Among them, four varistors R_1, R_2, R_3 and R_4 form a Wheatstone bridge structure.

When supplying power from a constant voltage source, the output voltage of the Wheatstone bridge is as follows:

$$V_{POUT} = V_{POUT2} - V_{POUT1} = \frac{R_1 R_3 - R_2 R_4}{(R_1 + R_2)(R_3 + R_4)} \cdot V_{DD}. \quad (6)$$

In the formula, V_{DD} is the working voltage and V_{POUT} is the output voltage. In an ideal state, the resistance of the four

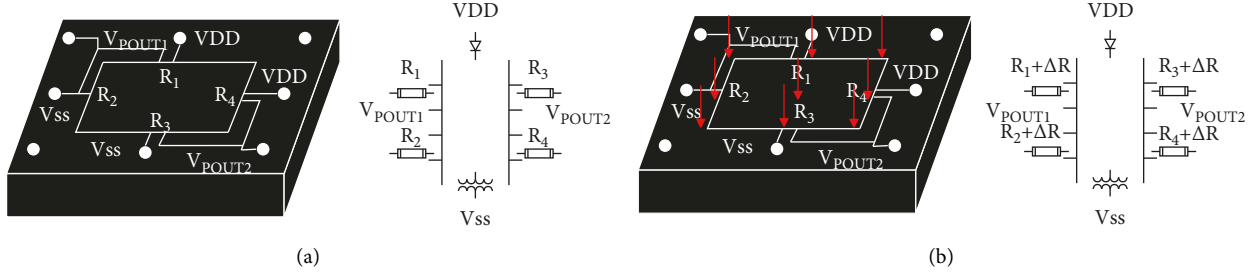


FIGURE 2: Schematic diagram of the working principle of the pressure sensor: (a) $P = 0$ kPa; (b) $P = 0$ kPa.

varistors is the same. When there is no pressure, the resistance does not change, so the output voltage of the Wheatstone bridge is zero, as shown in Figure 2(a).

When the sensor is under pressure, the silicon membrane deforms elastically. Due to the piezoresistive effect, the four varistors are under stress and the resistance values change. The resistance value of R_1, R_3 decreases by ΔR , and the resistance value of R_2, R_4 increases by ΔR , that is, $R_1 \rightarrow R_1 \cdot \Delta R, R_2 \rightarrow R_2 \cdot \Delta R, R_3 \rightarrow R_3 \cdot \Delta R, R_4 \rightarrow R_4 \cdot \Delta R$, as shown in Figure 2(b). As a result, the Wheatstone bridge loses its balance and produces an output voltage:

$$V_{POUT} = V_{POUT2} - V_{POUT1}$$

$$= \frac{(R_1 - \Delta R)(R_3 - \Delta R) - (R_2 + \Delta R)(R_4 + \Delta R)}{(R_1 - \Delta R + R_2 + \Delta R)(R_3 - \Delta R + R_4 + \Delta R)} \cdot V_{DD}, \quad (7)$$

$$V_{POUT} = V_{POUT2} - V_{POUT1} = \frac{\Delta R}{R} \cdot V_{DD}. \quad (8)$$

From (8), it can be seen that the output voltage of the Wheatstone bridge is proportional to $\Delta R/R$ and, at the same time, proportional to the operating voltage V_{DD} . The rate of change of the resistance of the monocrystalline silicon resistance is determined by the following formula [23]:

$$\frac{\Delta R}{R} = \pi_1 \sigma_1 + \pi_{\perp} \sigma_{\perp}. \quad (9)$$

In the formula, π_1 is the longitudinal piezoresistive coefficient and π_{\perp} is the transverse piezoresistive coefficient, both of which are related to the crystal orientation. It can be seen that when the crystal orientation is selected, the output voltage of the pressure sensor is proportional to the stress of the varistor.

The three-axis acceleration sensor is based on the piezoresistive effect of semiconductor materials. Varistors are fabricated at the roots of the four L-shaped beams and the middle double beams, and they are connected to form a Wheatstone bridge structure. The acceleration is measured by measuring the output voltage of the Wheatstone bridge.

Figure 3 shows the structure diagram of the acceleration sensor in the z -axis direction. The four varistors $R_1, R_2, R_3,$ and R_4 on the middle double beam structure form a Wheatstone bridge.

When supplying power from a constant voltage source, the output voltage of the Wheatstone bridge is as follows:

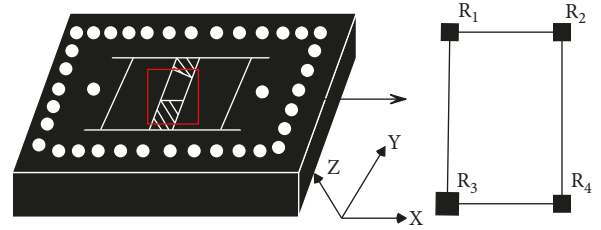


FIGURE 3: Schematic diagram of the z -axis structure of the acceleration sensor.

$$V_{ZOUT} = V_{ZOUT2} - V_{ZOUT1} = \frac{R_{z1}R_{z3} - R_{z2}R_{z4}}{(R_{z1} + R_{z2})(R_{z3} + R_{z4})} \cdot V_{DD}, \quad (10)$$

In the formula, V_{DD} is the working voltage and V_{ZOUT} is the output voltage. In an ideal state, the resistance of the four varistors is the same, and when there is no acceleration, the resistance does not change, so the output voltage of the Wheatstone bridge is zero, as shown in Figure 4(a).

When the sensor is subjected to acceleration in the z -axis direction, the beam deforms. Due to the piezoresistive effect, the four varistors are under stress and the resistance values change. The resistance values of R_{z1} and R_{z4} decrease by ΔR , and the resistance values of R_{z2} and R_{z3} increase by ΔR , that is, $R_{z1} \rightarrow R_{z1} \cdot \Delta R, R_{z2} \rightarrow R_{z2} \cdot \Delta R, R_{z3} \rightarrow R_{z3} \cdot \Delta R, R_{z4} \rightarrow R_{z4} \cdot \Delta R$, as shown in Figure 4(b). As a result, the Wheatstone bridge loses its balance and produces an output voltage:

$$V_{ZOUT} = V_{ZOUT2} - V_{ZOUT1}$$

$$= \frac{(R_{z1} - \Delta R)(R_{z3} - \Delta R) - (R_{z2} + \Delta R)(R_{z4} + \Delta R)}{(R_{z1} - \Delta R + R_{z2} + \Delta R)(R_{z3} - \Delta R + R_{z4} + \Delta R)} \cdot V_{DD}, \quad (11)$$

$$V_{ZOUT} = V_{ZOUT2} - V_{ZOUT1} = \frac{\Delta R}{R} \cdot V_{DD}. \quad (12)$$

The working principle of the x - and y -axis directions of the three-axis acceleration sensor is similar to that of the z -axis. Figure 5 shows a schematic diagram of the structure of the acceleration sensor in the x and y -axis directions. The varistors R_{x1}, R_{x2}, R_{x3} and R_{x4} on the L-shaped beam structure constitute the Wheatstone bridge for x -axis detection and R_{y1}, R_{y2}, R_{y3} and R_{y4} constitute the Wheatstone bridge for y -axis detection. In an ideal state, since the resistance of the varistor is the same, the output voltage of the Wheatstone bridge is zero when there is no acceleration.

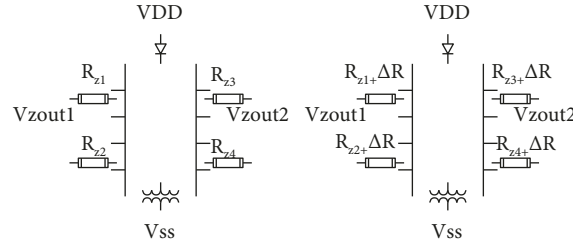


FIGURE 4: Schematic diagram of the working principle of the acceleration sensor in the z -axis direction: (a) $a_z=0$ and (b) $a_z \neq 0$.

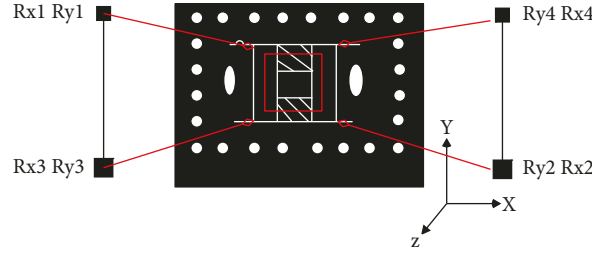


FIGURE 5: Schematic diagram of the x and y -axis structure of the acceleration sensor.

When the sensor is subjected to acceleration in the x -axis or y -axis direction, the L-shaped beam deforms. Due to the piezoresistive effect, the resistance of the varistor changes.

Figures 6(a) and 6(b) show schematic diagrams of the working principle of the x and y axes, respectively. The Wheatstone bridge loses balance and produces an output voltage.

$$V_{XOUT} = V_{XOUT2} - V_{XOUT1} = \frac{(R_{x1} - \Delta R)(R_{x3} - \Delta R) - (R_{x2} + \Delta R)(R_{x4} + \Delta R)}{(R_{x1} - \Delta R + R_{x2} + \Delta R)(R_{x4} - \Delta R + R_{x3} + \Delta R)} \cdot V_{DD},$$

$$V_{XOUT} = V_{XOUT2} - V_{XOUT1} = \frac{\Delta R}{R} \cdot V_{DD},$$

$$V_{rOUT} = V_{rOUT2} - V_{rOUT1} = \frac{(R_{x1} - \Delta R)(R_{x4} - \Delta R) - (R_{x2} + \Delta R)(R_{x3} + \Delta R)}{(R_{x1} - \Delta R + R_{x2} + \Delta R)(R_{x4} - \Delta R + R_{x3} + \Delta R)} \cdot V_{DD},$$

$$V_{rOUT} = V_{rOUT2} - V_{rOUT1} = \frac{\Delta R}{R} \cdot V_{DD}.$$

(13)

According to the Hall effect theory, magnetic field sensor characteristic simulation, and process design, Figure 7 shows a schematic diagram of the Hall magnetic field sensor structure. Among them, I_1 and I_2 are control current poles, V_{H1} and V_{H2} are two Hall output terminals, W is the width of the magnetic sensitive layer, and L is the length of the magnetic sensitive layer.

In this paper, the Hall magnetic sensitive layer has a width of $160\mu\text{m}$ and a length of $320\mu\text{m}$. The n-type lightly doped by an ion implantation process is used to form an n-type conductive layer with electrons as the majority carrier. The Hall output terminal is located at the center position on both sides of the magnetic sensitive layer, and the size is $12 \times 12 \mu\text{m}^2$, the control current pole size is $160 \times 50 \mu\text{m}^2$, and the ion implantation process is used for n-type heavy doping.

According to the theoretical formula of magnetic field sensor sensitivity (14),

$$V_H = V_{H1} - V_{H2} = \mu \cdot \frac{W}{L} \cdot V_{DD} \cdot f_H \left(\frac{L}{W}, \theta \right). \quad (14)$$

Ideally, when the power supply voltage V_{DD} is 5.0V , the electron mobility μ_n is $1400\text{cm}^2/(\text{V}\cdot\text{s})$, and the geometric structure factor $f_H(L/W, \theta)$ is 1, the theoretical sensitivity of the magnetic field sensor is about 350mVT .

According to the piezoresistive effect theory, pressure sensor characteristic simulation, and process design, Figure 8 shows a schematic diagram of the Hall magnetic field sensor structure. Among them, R_1, R_2, R_3 and R_4 are four varistors, and b is the side length of the square silicon membrane of the pressure sensor. In order to take into account multiple sensor size designs in a limited chip area, the pressure sensor square silicon film size is set to $1500 \times 1500 \mu\text{m}^2$.

The rectangular coordinate system is established with the center of the square silicon film as the origin, as shown in Figure 9. The x -axis is the crystal orientation of single crystal

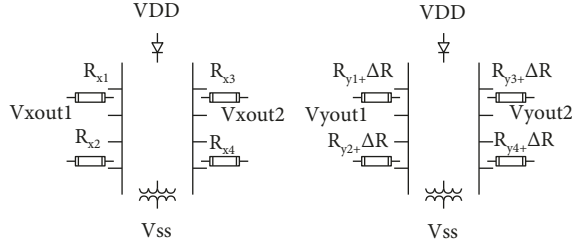


FIGURE 6: Schematic diagram of the working principle of the x -axis and y -axis of the acceleration sensor: (a) x -axis; (b) y -axis.

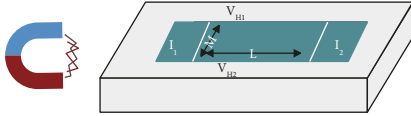


FIGURE 7: Basic structure of magnetic field sensor.

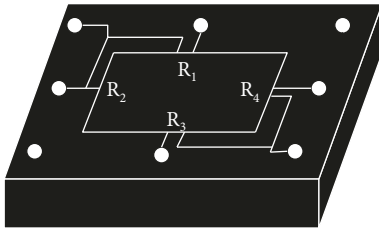


FIGURE 8: Schematic diagram of the magnetic field sensor structure.

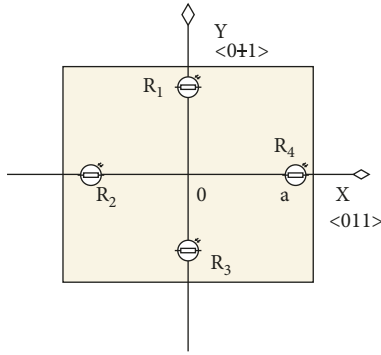


FIGURE 9: Schematic diagram of the shape of the silicon film.

silicon $\langle 011 \rangle$, and the y -axis is the crystal orientation of single crystal silicon $\langle 0\bar{1}1 \rangle$. The four varistors are placed along the direction parallel to the crystal $\langle 0\bar{1}1 \rangle$ direction. Among them, a is the distance from the center of the silicon film to the edge of the silicon film, that is, the half-length of the silicon film. The stress on the upper surface of the square silicon film is as follows:

$$\begin{aligned} \sigma_{xx} &= \frac{-96P}{96} \left(\frac{a}{h}\right)^2 \left[\left(\frac{3x^2}{a^2} - 1\right) \left(\frac{y^2}{a^2} - 1\right) + \mu \left(\frac{3y^2}{a^2} - 1\right) \left(\frac{x^2}{a^2} - 1\right) \right], \\ \sigma_{yy} &= \frac{-49P}{96} \left(\frac{a}{h}\right)^2 \left[\left(\frac{3y^2}{a^2} - 1\right) \left(\frac{x^2}{a^2} - 1\right) + \mu \left(\frac{3x^2}{a^2} - 1\right) \left(\frac{y^2}{a^2} - 1\right) \right]. \end{aligned} \quad (15)$$

In the formula, P is the applied pressure, μ is the Poisson's ratio, and h is the thickness of the square silicon film.

For pressure sensors based on the piezoresistive effect, the absolute value of the relative change in the resistance of the varistor that constitutes the Wheatstone bridge should be equal, that is,

$$\left| \frac{\Delta R_1}{R_1} \right| = \left| \frac{\Delta R_2}{R_2} \right| = \left| \frac{\Delta R_3}{R_3} \right| = \left| \frac{\Delta R_4}{R_4} \right|. \quad (16)$$

In order to improve the sensitivity of the sensor, the varistor should be designed at the position where the absolute value of the difference between the longitudinal stress and the transverse stress of the square silicon film is the largest.

Through further theoretical calculations, the coordinate values of the varistors R_2 and R_4 can be obtained. Since the varistors R_2 and R_4 are symmetrical along the y axis, only the coordinate value of R_4 needs to be calculated. The coordinates at both ends of R_1 are $(0, y_1)$ and $(0, y_2)$, respectively. The coordinates of both ends of R_4 are $(n, -L/2)$, $(n, L/2)$, L is the length of the varistor, W is the width of the varistor, and n is the coordinate value of R_4 on the x -axis. According to the formula, the average longitudinal stress of the varistor R and R can be obtained as follows:

$$\begin{aligned} (\bar{\sigma}_l)_1 &= \bar{\sigma}_{yy} = \frac{\int_{y_1}^{y_2} \sigma_{yy} dy}{\int_{y_1}^{y_2} dy} = \frac{1}{L} \int_{y_1}^{y_2} \sigma_{yy} dy \\ &= \frac{49}{96} \frac{P}{a^4 h^2 L} \int_{y_1}^{y_2} \left[\mu(3x^2 - a^2)(y^2 - a^2)^2 + (3y^2 - a^2)(x^2 - a^2)^2 \right] dy, \\ (\bar{\sigma}_l)_4 &= \bar{\sigma}_{yy} = \frac{\int_{L/2}^{L/2} \sigma_{yy} dy}{\int_{L/2}^{L/2} dy} = \frac{1}{L} \int_{L/2}^{L/2} \sigma_{yy} dy \\ &= \frac{49}{96} \frac{P}{a^4 h^2 L} \int_{L/2}^{L/2} \left[\mu(3x^2 - a^2)(y^2 - a^2)^2 + (3y^2 - a^2)(x^2 - a^2)^2 \right] dy. \end{aligned} \quad (17)$$

In the same way, according to formula (12), the average transverse stress of varistor R_1 and R_4 can be obtained as follows:

$$\begin{aligned} (\bar{\sigma}_t)_1 &= \bar{\sigma}_{xx} = \frac{\int_{x_1}^{x_2} \sigma_{xx} dx}{\int_{x_1}^{x_2} dx} = \frac{1}{W} \int_{x_1}^{x_2} \sigma_{xx} dx \\ &= \frac{49}{96} \frac{P}{a^4 h^2 W} \int_{x_1}^{x_2} \left[(3x^2 - a^2)(y^2 - a^2)^2 + \mu(3y^2 - a^2)(x^2 - a^2)^2 \right] dx, \\ (\bar{\sigma}_t)_4 &= \bar{\sigma}_{xx} = \frac{\int_{x_1}^{x_2} \sigma_{xx} dx}{\int_{x_1}^{x_2} dx} = \frac{1}{W} \int_{x_1}^{x_2} \sigma_{xx} dx \\ &= \frac{49}{96} \frac{P}{a^4 h^2 W} \int_{x_1}^{x_2} \left[(3n^2 - a^2)(y^2 - a^2)^2 + \mu(3y^2 - a^2)(n^2 - a^2)^2 \right] dx. \end{aligned} \quad (18)$$

The absolute value of the difference between the longitudinal stress and the transverse stress of the varistor R_1 and R_4 shall satisfy the following:

$$|(\bar{\sigma}_l)_1 - (\bar{\sigma}_t)_1| = |(\bar{\sigma}_l)_4 - (\bar{\sigma}_t)_4|. \quad (19)$$

In this paper, the values of the above physical quantities are brought into (19), and the coordinate of the varistor R_4 on the x -axis is $n = 704$, so R_4 should be made $46 \mu\text{m}$ away from the edge of the silicon film.

According to the piezoresistive effect theory, acceleration sensor characteristic simulation, and process design, Figure 10 shows a schematic diagram of the three-axis acceleration sensor structure. Among them, R_{x1}, R_{x2}, R_{x3} and R_{x4} are varistors in the x -axis direction, R_{y1}, R_{y2}, R_{y3} and R_{y4} are varistors in the y -axis direction, and R_{z1}, R_{z2}, R_{z3} and R_{z4} are varistors in the z -axis direction. The length of the L-shaped beam is $1600 \mu\text{m}$, the width is $200 \mu\text{m}$, the length of the middle double beam is $300 \mu\text{m}$, and the width is $150 \mu\text{m}$.

From the working principle of the three-axis acceleration sensor and the ANSYS simulation analysis, it can be seen that the area sensitive to acceleration in the x -axis direction is located at the root of the L-shaped beam, and the stress on the outside is the largest, and it gradually decreases toward the inside. The area sensitive to acceleration in the y -axis direction is located at the root of the L-beam, and the stress in the center is the largest and gradually decreases to both sides; the area sensitive to acceleration in the z -axis direction is located at the root of the middle double-beam structure. Therefore, the varistor should be made at the corresponding maximum stress position.

The Euler method used in the algorithm for numerical integration is an explicit expression. Compared with the multistep method and the implicit method, it is simple to calculate, takes less time, and is easy to implement. However, due to the requirements of integration accuracy, especially stability requirements, the implicit formula should be used. In particular, when the ordinary differential equation has a rigid problem, a large time step can lead to numerical instability problems. Generally speaking, the implicit method has a larger absolute stability region than the explicit method, so this section discusses the influence of different numerical integration methods on the IEB-PF algorithm and PFF.

We assume that the initial conditions satisfy the following conditions:

$$\begin{cases} f(x, \lambda) = f(t, x) = \frac{dx}{dt}, \\ x(t_0) = x_0. \end{cases} \quad (20)$$

Common numerical integration methods can be divided into single-step method and multistep methods, explicit and implicit. If only the value at time n is used to solve x_{n+1} , it is called a single-step method, which is a self-starting algorithm. If the value at time $n - 1, n - 2 \dots$ needs to be used, it is called a multistep method, which is an algorithm that cannot be started by itself. The difference between explicit and implicit is that when solving x_{n+1} , the value at time $n+1$ is implicit, and the value before time $n+1$ is explicit expression.

We use the Taylor series to analyze the accuracy of numerical integration and assume that $x(t_n)$ is accurate and $t_{n+1} = t_n + h, h$ is the integration time step. The Taylor expansion at t_n has the following:

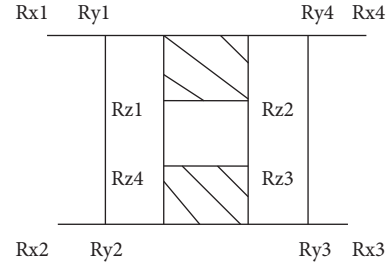


FIGURE 10: Basic structure of three-axis acceleration sensor.

$$\begin{aligned} x(t_{n+1}) = & x(t_n) + hx^{(1)}(t_n) + \frac{h^2}{2}x^{(2)}(t_n) \\ & + \dots + \frac{h^r}{r!}x^{(r)}(t_n) + O(h^{r+1}). \end{aligned} \quad (21)$$

- (1) Euler's method is the simplest numerical integration method commonly used, which converts a differential equation into an algebraic equation by using the difference quotient instead of the differential quotient. Euler's method is an explicit method. Due to the rigidity of ordinary differential equations, it is necessary to choose the integration time step reasonably. For Euler's method, there are the following:

$$x(t_{n+1}) = x(t_n) + hf(t_n, x_n). \quad (22)$$

Among them, t_n is the n time. From the expression of formula (2), it can be seen that the Euler method only retains the first two items of the Taylor expansion. Geometrically, Euler's method uses the area of the left rectangle to solve the integral. The local truncation error of Euler's method is $O(h^2)$, and the overall error is $O(h)$.

- (2) Modified Euler. The advantage of Euler's method is that it has a small amount of calculation, but at the same time because it ignores high-order terms, the accuracy is relatively low. From a geometrical point of view, it can be seen that compared with Euler's method, modified Euler's method uses the trapezoidal area to calculate integral and has higher accuracy:

$$x(t_{n+1}) = x(t_n) + \frac{h}{2} (f(t_n, x(t_n)) + f(t_{n+1}, x(t_{n+1}))). \quad (23)$$

It can be seen from formula (23) that the modified Euler method is an implicit expression, which is the arithmetic mean of the explicit Euler method and the implicit Euler method. The modified Euler method is a prediction-correction method, which needs to be solved iteratively, and the estimated value x_{n-1}' of x_{n+1} is obtained by using the Euler method and then substituted into the formula (23) to obtain the correction value:

$$\begin{cases} x'(t_{n+1}) = x(t_n) + hf(t_n, x(t_n)), \\ x(t_{n+1}) = x(t_n) + \frac{h}{2}(f(t_n, x(t_n)) + f(t_{n+1}, x'(t_{n+1}))). \end{cases} \quad (24)$$

Compared with the Euler method, the modified Euler method has higher accuracy, its local truncation error is $O(h^3)$, and the overall error is $O(h^2)$.

- (3) Runge-Kutta method. It can be seen from equation (2) that the more reserved terms of the Tate expansion, the higher the precision of the numerical integration, but the higher-order derivative of the function needs to be calculated. Therefore, a direct calculation is not convenient. The 4th-order Runge-Kutta method is one of the most commonly used methods to avoid higher-order derivative calculations:

$$\begin{cases} x(t_{n+1}) = x(t_n) + \frac{h}{6}(k_1 + 2k_2 + 2k_3 + k_4), \\ k_1 = f(t_n, x(t_n)), \\ k_2 = f\left(t_n + \frac{h}{2}, x(t_n) + \frac{h}{2}k_1\right), \\ k_3 = f\left(t_n + \frac{h}{2}, x(t_n) + \frac{h}{2}k_2\right), \\ k_4 = f(t_n + h, x(t_n) + hk_3). \end{cases} \quad (25)$$

The local truncation error of the fourth-order Runge-Kutta method is $O(h^5)$, and the overall error is $O(h^4)$.

- (4) Adams method (Adams). Adams' method is a linear multistep method with explicit and implicit expressions. The implicit method increases the amount

of computation, but the stability region is larger than that of the explicit formula, and for the Adams method of the same order, the accuracy of the implicit formula is often greater than that of the explicit formula. Therefore, the fourth-order form using the combination of explicit and implicit is as follows:

$$\begin{cases} x_{n+1}^p = x_n + \frac{h}{24}(55f(t_n, x_n) - 59f(t_{n-1}, x_{n-1}) + 37f(t_{n-2}, x_{n-2}) - 9f(t_{n-3}, x_{n-3})), \\ x_{n+1} = x_n + \frac{h}{24}(9f(t_{n+1}, x_{n+1}^p) + 19f(t_n, x_n) - 5f(t_{n-1}, x_{n-1}) + f(t_{n-2}, x_{n-2})). \end{cases} \quad (26)$$

It can be seen from formula (7) that the Adams method is also a prediction-correction method. It needs to use the single-step method of the same order to find the first few points. The local truncation error is $O(h^5)$, and the overall error is $O(h^4)$.

Resampling is an important part of the particle filter algorithm. Resampling can effectively alleviate the problem of particle weight degradation. At the same time, resampling also limits the parallel computing of particle filtering and also affects the computational efficiency of the algorithm when the number of particles is large. Different from resampling, particle redrawing is an optional solution in the IEB-PF algorithm and particle flow filtering. By constructing a homotopy function, particles can be moved to an accurate

position. However, due to the approximate calculation in the process of particle flow (in the parametric approximation method, the diffusion term and the constant term are ignored, the prior and the observation are assumed to be linear Gaussian distribution, and the weak form solution is solved), the particles cannot be accurately moved from the prior to the posterior. Therefore, repainting the particles, generating a new set of particles will help move the particles to the true posterior.

At present, there are few researches on particle repainting and its theoretical influence on particle flow filtering. It is mentioned in the literature that the mean value and covariance matrix of the posterior particles are used to redraw from the Gaussian distribution. The covariance

matrix is obtained by the EKF algorithm, but at the same time, the accuracy of the PFF algorithm will depend heavily on the EKF algorithm. Moreover, large errors will occur under the condition of high nonlinear intensity and non-Gaussian noise. There are two redrawing strategies. One is to redraw particles from a multivariate Gaussian distribution, where the mean is the posterior particle mean, and the covariance matrix is obtained by the shrinkage estimation method, which no longer relies on the EKF algorithm. The second method redraws from a mixture of Gaussian models. The mixture Gaussian model is estimated by the kernel density, and the particle distribution is not assumed in the second method. It is pointed out in the literature that the mixture Gaussian model has higher estimation accuracy but increases the computational burden.

Aiming at the above problems, this paper proposes a simple and easy-to-implement fitness-based particle redrawing method. This method does not need to assume the distribution of particles before redrawing. The particles after redrawing have the same distribution as those before redrawing, and it is easy to implement. The fitness function is set as follows:

$$f_{\text{fitness}}^i = \exp \left\{ -\text{sqrt} \left[\frac{(Z_t - Z_{\text{tpre}}^i) R^{-1} (Z_t - Z_{\text{tpre}}^i)}{c} \right] \right\}. \quad (27)$$

Among them, Z_1 is the observed value at time t , Z_{tpre} is the observed predicted value at time t , R is the covariance matrix of observation noise, and c is an empirical constant, which can be set according to the actual system. After obtaining the fitness of each particle, it is obtained by normalizing:

$$f' = \frac{f_{\text{fitness}}^i}{\sum_{i=1}^N f_{\text{fitness}}^i}. \quad (28)$$

The weighted mean is obtained for the particles whose fitness is normalized, and then the particles are shifted to a new distribution with the same mean. Therefore, the method proposed in this paper does not change the distribution form of the particle posterior.

4. Motion Capture System for Sports Dance Teaching Based on Digital Filtering Algorithm

Three-dimensional animation technology can be displayed from multiple angles and gives people an immersive feeling, so it is more and more used in film and television works and character animation. The role performance in film and television animation needs to complete many complex actions. Even production with animation software will consume a lot of time, manpower, and financial resources, and it is sometimes difficult to make certain complex actions accurately. However, the use of motion capture technology can achieve precise, smooth, and detailed effects. It can be said that the current film and television animation works are not drawn but performed. Figure 11 is the workflow of the motion capture system for sports dance teaching.

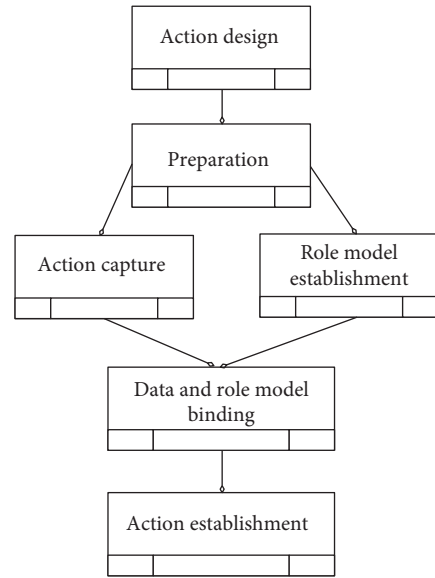


FIGURE 11: Workflow of the motion capture system for sports dance teaching.

Motion capture technology is continuously used in sports dance and other projects to assist the digitalization and scientification of sports dance. Compared with traditional sports dance teaching, motion capture technology can capture dancers' movements in real time, accurately record the movements of dancers' limbs in three-dimensional space, and digitize them for easy analysis and long-term storage. This measurement process can reduce the error caused by subjective factors, can measure a large amount of data information from multiple angles at the same time, and can provide real-time, accurate, and vivid teaching feedback. The data obtained can also be analyzed and designed, and its value can be explored in depth to produce materials suitable for self-learning. Therefore, in the process of sports education and teaching, combining motion capture technology with traditional teaching can solve the drawbacks and problems in traditional teaching, improve teaching quality and learning efficiency, and has high research significance and practical value. The movement flow of sports dance based on motion capture is shown in Figure 12.

Undergraduates majoring in dance generally have many years of dance foundation and have a good understanding of dance body rhyme skills. It is easier for them to learn dance by themselves, but only through a single angle of video learning, many complex and delicate movements are difficult to master, and the time is very long. With the help of motion capture technology, it will be much easier for dance majors to learn national dance by themselves, as shown in Figure 13.

The motion capture system of sports dance teaching based on a digital filtering algorithm adopts a three-layer system design method, which are the data layer, control layer, and presentation layer. (1) The data layer is mainly responsible for reading music configuration files and evaluation standard configuration files, using the iterator as the middle abstract layer to provide convenient data access

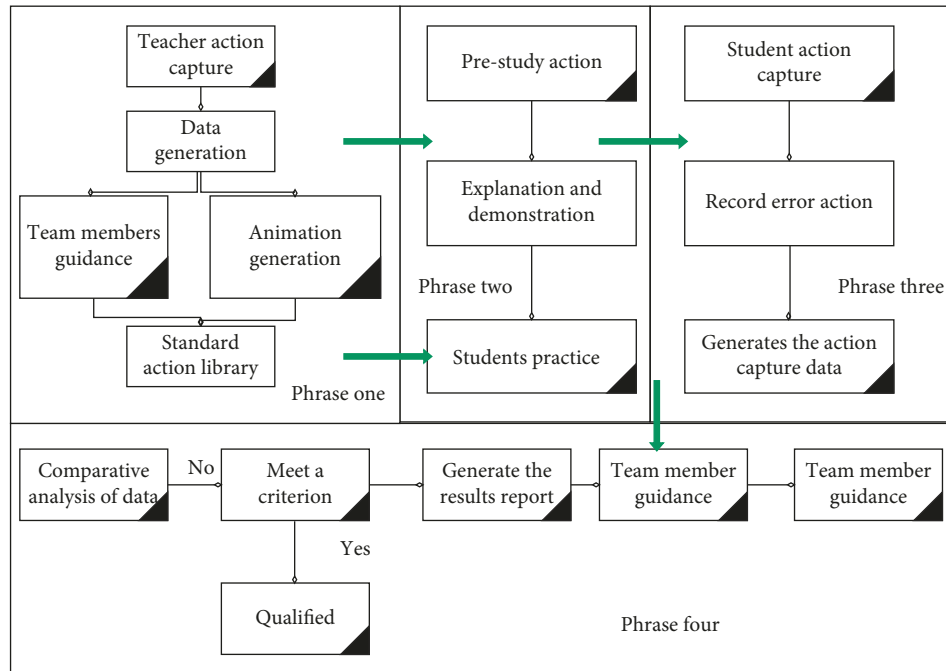


FIGURE 12: Sports dance movement process based on motion capture.

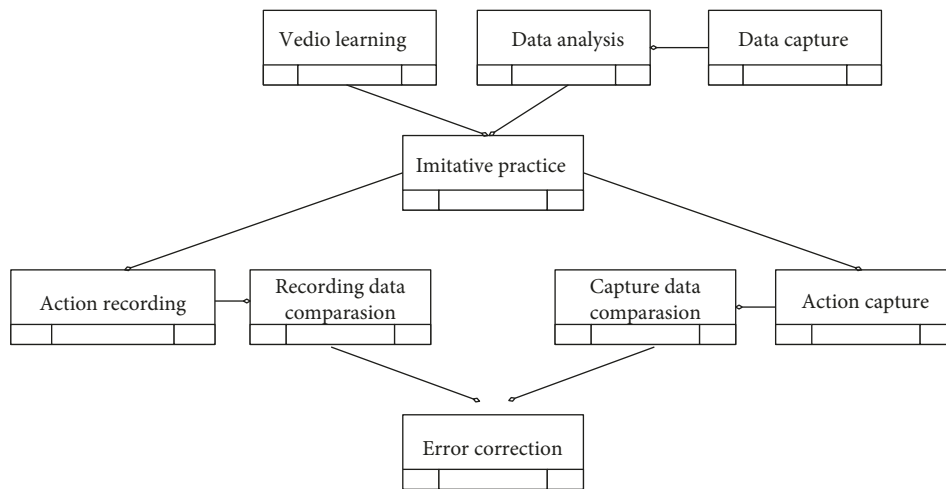


FIGURE 13: Motion capture system for sports dance teaching based on digital filtering algorithm.

interfaces for the control layer and the presentation layer. Among them, the song configuration file stores each song's beat type, number of beats, beat interval for action similarity evaluation and beat interval displayed by action prompt pictures. The evaluation standard file stores the action similarity score and the corresponding relationship with its level. (2) The control layer includes music beat control, action sequence preprocessing, action similarity evaluation, and dance flow control system. The action sequence preprocessing module uses an interpolation wavelet to denoise the collected action sequence. The action similarity evaluation module scores user actions in real time. The beat control module is based on the song configuration and the time manager of the Unity3D engine and passes the strong

and weak beat messages to the action evaluation module and some modules of the performance layer. The dance process control module is responsible for the overall process control, including the synchronization of music and dance animation, pause, and dance end judgment. (3) The presentation layer includes visual elements and user interfaces in the three-dimensional scene, which is used to receive and display data input by users, and provide users with somatosensory virtual interactive scenes. Among them, the user points module is used to accumulate and display the points of each action evaluation. The action prompt module is used to display the prompt diagram of the previous, current, and next action. The scene interaction module controls the synchronization of the three-dimensional model in the scene

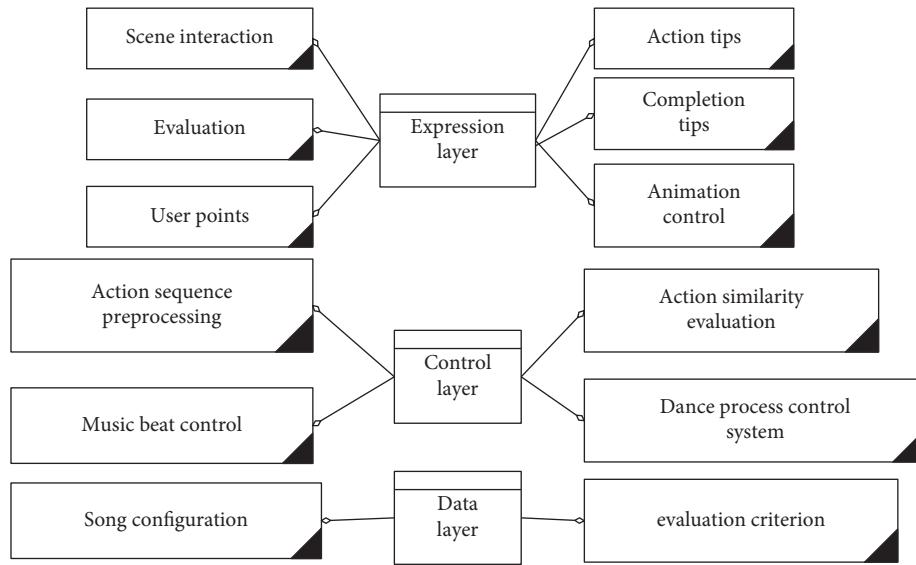


FIGURE 14: System structure diagram.

TABLE 1: System experiment results.

Number	Digital filtering	Motion capture	Number	Digital filtering	Motion capture
1	94.57	82.52	22	97.34	93.14
2	94.89	93.32	23	95.71	89.51
3	97.41	93.77	24	94.94	90.33
4	96.72	83.70	25	97.52	92.13
5	96.33	84.56	26	94.16	87.53
6	96.18	84.72	27	94.68	87.02
7	95.50	93.00	28	95.53	94.04
8	97.85	94.27	29	95.06	89.77
9	95.20	84.50	30	96.07	89.73
10	96.20	94.91	31	97.11	92.00
11	96.16	87.87	32	95.62	84.77
12	96.81	88.39	33	97.46	88.57
13	96.99	90.55	34	95.68	90.70
14	97.36	92.13	35	95.92	86.51
15	96.44	94.71	36	94.09	92.36
16	97.10	83.81	37	95.78	88.51
17	95.17	94.11	38	97.84	86.62
18	97.31	91.21	39	95.40	87.49
19	96.72	94.08	40	94.63	82.03
20	97.25	87.28	41	97.03	85.34
21	97.58	85.72	42	95.59	88.87

with the user's actions. The evaluation display module is used to display the evaluation of the user's dance movements in real time, and the data comes from the action evaluation module of the logic layer. The completion degree display module is used to let the user know the completion degree of the current song. The animation control module realizes the playback of standard dance movements collected by the motion capture system on the three-dimensional model. The system structure is shown in Figure 14.

After constructing the above system, the performance of the system is verified, and the digital filtering and motion capture of sports dance teaching is verified, and the results are shown in Table 1 and Figure 15.

From the above research, it can be seen that the motion capture system for sports dance teaching based on the digital filter algorithm proposed in this paper can play an important role in sports dance teaching and effectively improve the efficiency of sports dance teaching.

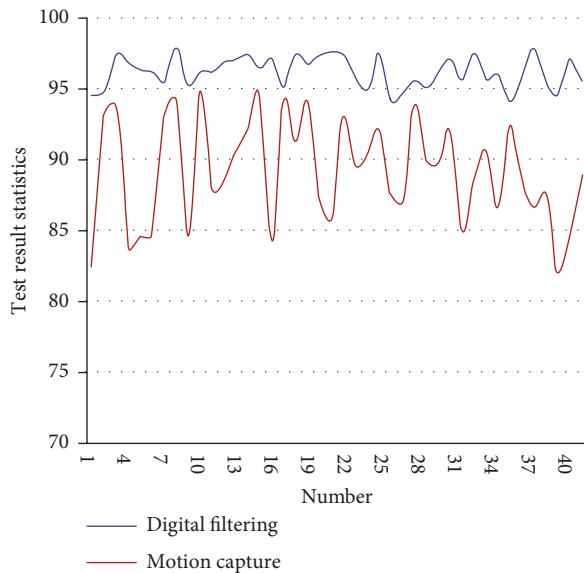


FIGURE 15: System performance statistics.

5. Conclusion

In domestic sports dance education, the emergence of virtual technology provides the possibility for the innovation of sports dance education in colleges and universities. Virtual reality can be combined with sports dance education, and new technologies can be used to expand students' knowledge and increase their knowledge of sports dance background. Moreover, it can arouse students' learning fun, display sports dance for students from various angles, and help students understand the connotation of sports dance education. The combination of virtual technology and sports dance education includes the collection and display of virtual data. Through data collection of sports dance professionals, a database of sports dance teaching is established, and motion capture and collection techniques are used to virtualize sports dance characters and further abstract them into digital sports dance. It can evaluate and correct students' movements. In addition, combining with music, stage design, text, etc., can enhance the integration of sports dance art and other arts, for virtual display, and even on-site virtual projection. At the same time, it provides three-dimensional teaching and exhibition space for sports dance teaching and increases students' interest and professional perception. This article combines the digital filtering algorithm to construct the sports dance teaching motion capture system, changes the current sports dance teaching method, applies intelligent teaching to the sports dance motion capture, and improves the teaching effect of sports dance teaching.

Data Availability

The labeled dataset used to support the findings of this study is available from the corresponding author upon request.

Conflicts of Interest

The author declares no competing interests.

References

- [1] J. Xu, K. Tasaka, and M. Yamaguchi, "[Invited paper] fast and accurate whole-body pose estimation in the wild and its applications," *ITE Transactions on Media Technology and Applications*, vol. 9, no. 1, pp. 63–70, 2021.
- [2] G. Szűcs and B. Tamás, "Body part extraction and pose estimation method in rowing videos," *Journal of Computing and Information Technology*, vol. 26, no. 1, pp. 29–43, 2018.
- [3] R. Gu, G. Wang, Z. Jiang, and J.-N. Hwang, "Multi-person hierarchical 3d pose estimation in natural videos," *IEEE Transactions on Circuits and Systems for Video Technology*, vol. 30, no. 11, pp. 4245–4257, 2020.
- [4] M. Nasr, R. Osama, H. Ayman, N. Mosaad, N. Ebrahim, and A. Mounir, "Realtime multi-person 2D pose estimation," *International Journal of Advanced Networking and Applications*, vol. 11, no. 6, pp. 4501–4508, 2020.
- [5] N. T. Thành, L. V. Hùng, and P. T. Công, "An evaluation of pose estimation in video of traditional martial arts presentation," *Journal of Research and Development on Information and Communication Technology*, vol. 2019, no. 2, pp. 114–126, 2019.
- [6] I. Petrov, V. Shakhuro, and A. Konushin, "Deep probabilistic human pose estimation," *IET Computer Vision*, vol. 12, no. 5, pp. 578–585, 2018.
- [7] G. Hua, L. Li, and S. Liu, "Multipath affine stacked-hourglass networks for human pose estimation," *Frontiers of Computer Science*, vol. 14, no. 4, Article ID 144701, 2020.
- [8] K. Aso, D. H. Hwang, and H. Koike, "Portable 3D human pose estimation for human-human interaction using a chest-mounted fisheye camera," in *Proceedings of the Augmented Humans Conference 2021*, pp. 116–120, Rovaniemi Finland, February 2021.
- [9] D. Mehta, S. Sridhar, O. Sotnychenko et al., "VNect," *ACM Transactions on Graphics*, vol. 36, no. 4, pp. 1–14, 2017.
- [10] S. Liu, Y. Li, and G. Hua, "Human pose estimation in video via structured space learning and halfway temporal evaluation," *IEEE Transactions on Circuits and Systems for Video Technology*, vol. 29, no. 7, pp. 2029–2038, 2019.
- [11] S. Ershadi-Nasab, E. Noury, S. Kasaei, and E. Sanaei, "Multiple human 3d pose estimation from multiview images," *Multimedia Tools and Applications*, vol. 77, no. 12, Article ID 15573, 2018.
- [12] X. Nie, J. Feng, J. Xing, S. Xiao, and S. Yan, "Hierarchical contextual refinement networks for human pose estimation," *IEEE Transactions on Image Processing*, vol. 28, no. 2, pp. 924–936, 2019.
- [13] Y. Nie, J. Lee, S. Yoon, and D. S. Park, "A multi-stage convolution machine with scaling and dilation for human pose estimation," *KSII Transactions on Internet and Information Systems (TIIS)*, vol. 13, no. 6, pp. 3182–3198, 2019.
- [14] A. Zarkeshev and C. Csiszár, "Rescue method based on V2X communication and human pose estimation," *Periodica Polytechnica: Civil Engineering*, vol. 63, no. 4, pp. 1139–1146, 2019.
- [15] W. McNally, A. Wong, and J. McPhee, "Action recognition using deep convolutional neural networks and compressed spatio-temporal pose encodings," *Journal of Computational Vision and Imaging Systems*, vol. 4, no. 1, p. 3, 2018.
- [16] R. G. Diaz, F. Laamarti, and A. El Saddik, "DTCoach: your digital twin coach on the edge during COVID-19 and beyond," *IEEE Instrumentation and Measurement Magazine*, vol. 24, no. 6, pp. 22–28, 2021.

- [17] A. Bakshi, D. Sheikh, Y. Ansari, C. Sharma, and H. Naik, "Pose estimate based yoga instructor," *International Journal of Recent Advances in Multidisciplinary Topics*, vol. 2, no. 2, pp. 70–73, 2021.
- [18] S. L. Colyer, M. Evans, D. P. Cosker, and A. I. T. Salo, "A review of the evolution of vision-based motion analysis and the integration of advanced computer vision methods towards developing a markerless system," *Sports Medicine - Open*, vol. 4, no. 1, pp. 24–15, 2018.
- [19] I. Sarandi, T. Linder, K. O. Arras, and B. Leibe, "Metrabs: metric-scale truncation-robust heatmaps for absolute 3d human pose estimation," *IEEE Transactions on Biometrics, Behavior, and Identity Science*, vol. 3, no. 1, pp. 16–30, 2021.
- [20] A. Azhand, S. Rabe, S. Müller, I. Sattler, and A. Heimann-Steinert, "Algorithm based on one monocular video delivers highly valid and reliable gait parameters," *Scientific Reports*, vol. 11, no. 1, pp. 1–14, Article ID 14065, 2021.
- [21] J. Xu and K. Tasaka, "[Papers] keep your eye on the ball: detection of kicking motions in multi-view 4K soccer videos," *ITE Transactions on Media Technology and Applications*, vol. 8, no. 2, pp. 81–88, 2020.
- [22] Z. Li, J. Bao, T. Liu, and W. Jiacheng, "Judging the normativity of PAF based on TFN and NAN," *Journal of Shanghai Jiaotong University*, vol. 25, no. 5, pp. 569–577, 2020.
- [23] J. Bhombe, A. Jethwa, A. Singh, and T. Nagarhalli, "Review of pose recognition systems," *VIVA-Tech International Journal for Research and Innovation*, vol. 1, no. 4, pp. 1–8, 2021.